A discrete model for long time sintering

Stefan Luding [a,b,e] Karsten Manetsberger [c] Johannes Müllers [d]

[a] *Particle Technology, DelftChemTech, TU Delft, Julianalaan 136, 2628 BL Delft, The Netherlands*

[b] *Institut für Computeranwendungen 1, Universität Stuttgart, Pfaffenwaldring 27, 70569 Stuttgart, Germany*

[c] *Daimler Chrysler, Forschung und Technologie, Postfach 2360, 89013 Ulm, Germany*

[d] *Daimler Chrysler, Forschung und Technologie, Dornier GmbH, 88039 Friedrichshafen, Germany*

[e] *e-mail:* `s.luding@tnw.tudelft.nl`

Abstract

A discrete model for the sintering of polydisperse, inhomogeneous arrays of cylinders is presented with empirical contact force-laws, taking into account plastic deformations, cohesion, temperature dependence (melting), and long-time effects. Samples are prepared under constant isotropic load, and are sintered for different sintering times. Increasing both external load and sintering time leads to a stronger, stiffer sample after cooling down. The material behavior is interpreted from both microscopic and macroscopic points of view.

Among the interesting results is the observation that the coordination number, even though it has the tendency to increase, sometimes slightly decreases, whereas the density continuously increases during sintering – this is interpreted as an indicator of reorganization effects in the packing. Another result of this study is the finding that strongly attractive contacts occur during cool-down of the sample and leave a sintered block of material with almost equally strong attractive and repulsive contact forces.

Key words: Sintering, density and coordination number, compression test, yield stress, failure, discrete element model

1 Introduction

Before we discuss sintering and a discrete model for sintering, first we make some more philosophical remarks about continuous and discrete modeling

in general. In mechanics and physics there exist two ways to describe and model a particulate, inhomogeneous material like powder, ceramics or concrete. The first approach is based on continuum theory and relies on empirical assumptions about the macroscopic material behavior (Schwedes, 1968; Vermeer et al., 2001). For a summary of recent progress on the macroscopic modeling of sintering processes see the studies by Jagota et al. (1990); Jagota and Scherer (1995); Olevsky (1998); Bellehumeur et al. (1998); Zachariah and Carrier (1999); Riedel and Blug (2001); Manetsberger et al. (2001); Anestiev and Froyen (1999); Kraft et al. (2003) and the references therein. The macroscopic approach can be complemented by a "microscopic" description of the material on the particle or grain level, where the particles and their interactions are modeled one by one (Herrmann et al., 1998; DeLo et al., 1999; Vermeer et al., 2001). The former involves stress, strain and plastic yield conditions (Redanz and Fleck, 2001), whereas the latter deals with local force-deformation laws for each contact (Jagota and Dawson, 1990). The macroscopic approach neglects the microstructure due to its nature and often isotropy is assumed (Jagota et al., 1990). In contrast to finite element or network-models, or to models with a fixed topology, we will follow the path of a microscopic, dynamic modeling, where no assumptions about either geometry, topology, homogeneity, or isotropy of the powder packing are involved (DeLo et al., 1999; Heyliger and McMeeking, 2001; Redanz and Fleck, 2001).

However, we have to assume certain contact force-laws and, furthermore, will restrict ourselves to two dimensions. A clear disadvantage of discrete models is the limited number of particles that can be modeled with reasonable effort. Therefore, rather than examining large structures, we focus on small samples with a few hundred particles only.

In order to test the approach, a model system in a two-dimensional box filled with cohesive-frictional disks of different sizes, see Sec. 2, is examined by means of a "microscopic" discrete element method (DEM). The microscopic interaction model for plastic deformations, friction, and cohesion is discussed and time-, temperature-, and history-dependent behavior is introduced and rationalized in Sec. 3. The long time sintering of a block of material is simulated and the results are discussed in Sec. 4.

A final remark about units: Most of the quantities used in this paper imply SI units, and length is typically measured in meters, time in seconds, force in Newtons, that is mass times acceleration, and temperature in Kelvin (or degrees centigrade). Only for the pressure, a non-standard unit of Newton per meter is used, since we disregard the arbitrary length of the cylindrical particles.

2 Model System

One possibility to obtain information about the material behavior is to perform elementary tests in the laboratory. However, because it is difficult to observe what is going on inside the material, an alternative way is the simulations with the discrete element model (DEM) (Cundall and Strack, 1979; Bashir and Goddard, 1991; van Baars, 1996; Thornton and Antony, 2000; Thornton, 2000; Herrmann et al., 1998; Vermeer et al., 2001; Luding et al., 2000, 2001). The numerical "experiment" chosen is a bi-axial box set-up, see Fig. 1, where the left and bottom walls are fixed, and a stress- or strain-controlled deformation is applied to the other walls. In the future, quantitative agreement between experiment (Kraft et al., 2003) and simulation has to be achieved. However, this issue is far from the scope of this paper.

Stress control means that the wall is subject to a predefined external pressure that, in equilibrium, is cancelled by the stress, which the material exerts on the wall. In a typical "experiment", the particles are rapidly compressed with constant, isotropic pressure and then left alone for some time and at constant temperature, typically not much below the melting point.

The stress-controlled motion of the walls is described by the differential equation

$$m_{\mathrm{w}}\ddot{x}(t) = F_{\mathrm{w}}(t) - p_{\mathrm{w}}z(t) - \gamma_{\mathrm{w}}\dot{x}(t) \ , \tag{1}$$

where m_{w} is the mass of the wall. Values of m_{w} large as compared to the sample mass lead to slow adaptation and vibrations, whereas small values allow for a rapid adaptation to the actual situation. Three forces are active: (i) the force $F_{\mathrm{w}}(t)$ due to the bulk material, (ii) the force $-p_{\mathrm{w}}z(t)$ due to the external pressure, and (iii) a viscous force which damps the motion of the wall so that oscillations are reduced. Note that pressure is here measured in units of force per length, that is force per area times unit length of the cylindrical particles.

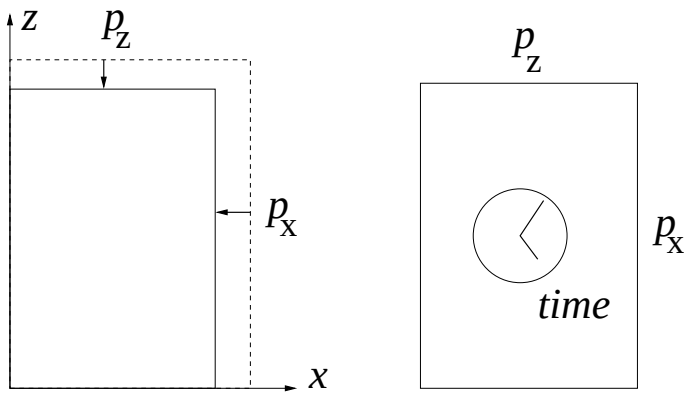

Fig. 1. (Left) Preparation of the sample with pressure on both sides. (Right) After the system is relaxed the evolution in time of the sample with time is examined.

Inside the system, N disks with radii a_i ($i = 1, \ldots, N$) and height h are placed. The radii are drawn from a homogeneous distribution with mean a_0 and relative width w_0 so that $a_i/a_0 \in [1 - w_0, 1 + w_0]$. The particle-particle interactions and the parameters involved are discussed in the next section.

3 Discrete Particle Model

The elementary units of granular materials are mesoscopic grains which deform under stress, possibly yield, change their properties with time, and can behave differently for different temperatures. Since the realistic modeling of the deformations of the particles is much too complicated to allow for a subsequent many-particle simulation, we relate the interaction force to the overlap δ of two particles, see Fig. 2. In the absence of long-range forces, an interaction takes place only if particles are in contact and thus $\delta > 0$. In that case, the forces are split into a normal and a tangential component denoted by indices n and t, respectively.

Note that the particles have a fixed radius for constant temperature. Thus a larger force leads to a larger overlap (model) corresponding to a larger deformation (reality). As long as overlap and deformation are much smaller than the particle radius, the deformation is local and the constant radius assumption makes sense for the rest of the particle.

If all forces $\boldsymbol{f}_i$ acting on the particle i, either from other particles, from boundaries or from external forces, are known, the problem is reduced to the integration of Newton's equations of motion for the translational and rotational degrees of freedom

$$m_i \frac{\mathrm{d}^2}{\mathrm{d}t^2} \boldsymbol{r}_i = \boldsymbol{f}_i \ , \quad \text{and} \quad I_i \frac{\mathrm{d}^2}{\mathrm{d}t^2} \boldsymbol{\varphi}_i = \boldsymbol{t}_i \ , \tag{2}$$

with the mass m_i of particle i, its position $\boldsymbol{r}_i$ the total force $\boldsymbol{f}_i = \sum_c \boldsymbol{f}_i^c$, its moment of inertia I_i, its angular velocity $\boldsymbol{\omega}_i = \mathrm{d}\boldsymbol{\varphi}_i/\mathrm{d}t$, the total torque $\boldsymbol{t}_i = \sum_c \boldsymbol{l}_i^c \times \boldsymbol{f}_i^c$, and the center-contact vector $\boldsymbol{l}_i^c$. The integration of the equations of motion is performed with a standard molecular dynamics Verlet algorithm together with Verlet-table neighborhood search (Allen and Tildesley, 1987).

3.1 Normal Contact Model

Two particles i and j at positions $\boldsymbol{r}_i$ and $\boldsymbol{r}_j$, with radii a_i and a_j, interact only if they are in contact so that their overlap

$$\delta = (a_i + a_j) - (\boldsymbol{r}_i - \boldsymbol{r}_j) \cdot \boldsymbol{n} \tag{3}$$

is positive, $\delta > 0$, with the unit vector $\boldsymbol{n} = \boldsymbol{n}_{ij} = (\boldsymbol{r}_i - \boldsymbol{r}_j)/|\boldsymbol{r}_i - \boldsymbol{r}_j|$ pointing from j to i. The force on particle i, from particle j can be written as $\boldsymbol{f}_{ij} = f_{ij}^n \boldsymbol{n} + f_{ij}^t \boldsymbol{t}$, with $\boldsymbol{n}$ perpendicular to $\boldsymbol{t}$. In this subsection, the normal forces are discussed.

3.1.1 Short time contact model

As first step, we discuss the time- and temperature-independent behavior of the contact forces between a pair of particles. For this, we modify and extend the linear hysteretic spring model (Walton and Braun, 1986; Luding, 1998; Tomas, 2000; Luding and Herrmann, 2001; Luding et al., 2003). It is the simplest version of some more complicated nonlinear-hysteretic force laws (Walton and Braun, 1986; Zhu et al., 1991; Sadd et al., 1993), which reflects the fact that at the contact point, plastic (permanent) deformations may take place. The repulsive (hysteretic) force can be written as

$$f_{ij} = \begin{cases} k_1 \delta & \text{loading,} \\ k_2(\delta - \delta_0) & \text{un/reloading,} \\ -k_c \delta & \text{unloading,} \end{cases} \tag{4}$$

with $k_1 \leq k_2$, see Fig. 2.

During the initial loading the force increases linearly with the overlap δ, until the maximum overlap $\delta_{\max}$ is reached, which is kept in memory as a *history parameter*. The line with slope k_1 thus defines the maximum force possible for a given δ. During unloading the force drops, on the line with slope k_2, from its value at $\delta_{\max}$ down to zero at the force-free overlap

$$\delta_0 = (1 - k_1/k_2)\delta_{\max} \ .$$

Reloading at any instant leads to an increase of the force along this line, until the maximum force is reached; for still increasing δ, the force follows again the line with slope k_1 and $\delta_{\max}$ has to be adjusted accordingly. Unloading below δ_0 leads to negative, attractive forces until at the overlap

$$\delta_{\min} = \frac{k_2 - k_1}{k_2 + k_c} \delta_{\max} \ ,$$

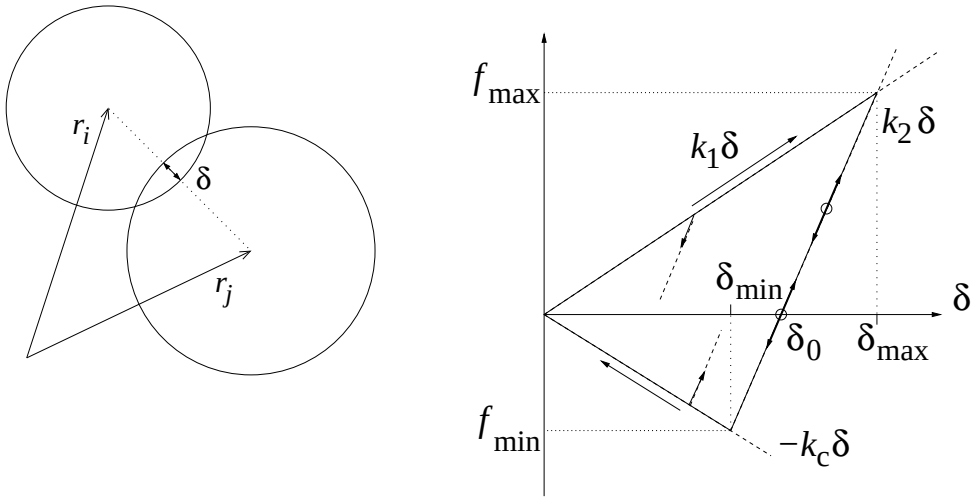

Fig. 2. (Left) Two particle contact with overlap δ. (Right) Force law for two springs with stiffness k_1 and k_2 for initial loading and subsequent un/reloading, respectively. Attractive forces are possible due to the cohesion strength k_c.

the minimum force $f_{\min} = -k_c\delta_{\min}$, i.e. the maximum attractive force, is obtained as a function of the model parameters k_1, k_2, k_c, and the history parameter $\delta_{\max}$. Further unloading leads to attractive forces on the branch $f = -k_c\delta$. [1]

The cone formed by the lines with slope k_1 and $-k_c$ defines the range of possible force values. If a force would fall outside the cone, it is forced to remain on the limit lines. Departure from these lines into the cone takes place in the case of unloading and reloading, respectively. Between these two extremes, unloading and reloading follow the same line with slope k_2. Possible equilibrium states are indicated as circles in Fig. 2, where the upper and lower circle correspond to a pre-stressed and stress-free state, respectively.

3.1.2 Viscous dissipation

In the case of collisions of particles and for large deformations, dissipation takes place due to the hysteretic nature of the force-law. For small displacements around some equilibrium state, the model does not contain dissipation. Therefore, in order to allow for stronger dissipation and thus faster relaxation, a viscous, velocity dependent dissipative force in normal direction,

$$f_{ij}^{n,\mathrm{d}} = \gamma_0 \dot{\delta} \ , \tag{5}$$

[1] The highest possible attractive force, for given k_1 and k_2, is reached for $k_c \to \infty$, so that $f_{\min} = -(k_2 - k_1)\delta_{\max}$. This would lead to a discontinuity at $\delta = 0$ that is avoided by using finite k_c.

is assumed with some damping coefficient γ_0. The half-period of a vibration around the equilibrium position, see Fig. 2, can be computed for arbitrary values of k_1 and k_c, as long as the overlap fulfills the condition $\delta_{\min} < \delta < \delta_{\max}$. In this case, k_2 determines the stiffness and one obtains a typical response time on the contact level (Luding, 1998),

$$t_c = \frac{\pi}{\omega} \ , \quad \text{with} \quad \omega = \sqrt{\frac{k_2}{m_{12}} - \eta_0^2} \ , \tag{6}$$

the eigenfrequency of the contact, the rescaled damping coefficient $\eta_0 = \gamma_0/(2m_{12})$, and the reduced mass $m_{12} = m_1 m_2/(m_1+m_2)$. The time-step of the simulation t_{MD} has to be chosen such that

$$t_{\mathrm{MD}} \approx t_c/50$$

for a proper integration of the equations of motion, so that we chose a typical time-step $t_{\mathrm{MD}} = \pi/(50\omega)$ after the model parameters k_2 and γ_0 are specified [2].

3.1.3 Stiffness increase with contact area

In order to account for the fact that a larger contact surface leads to a larger contact stiffness, the coefficient k_2 is made dependent on the maximum overlap history parameter $\delta_{\max}$ (and thus on the force-free overlap δ_0), as long as the overlap is below the threshold δ^{fluid} that corresponds to the "complete melting" of the particles. Complete melting is here the limit of an incompressible liquid that is contained in the model, however, neither discussed in detail nor verified for reasons of brevity.

The overlap δ^{fluid} corresponding to the stress-free fluid, is computed such that the volume fraction in the system equals unity. The volume fraction of a dense packing of rigid cylinders is

$$\nu_{\mathrm{solid}} = N\pi h a_0^2/V_{\mathrm{solid}} = \pi/(2\sqrt{3}) \ .$$

If all the material would be melted, the volume fraction is

$$\nu_{\mathrm{fluid}} = N\pi h a_0^2/V_{\mathrm{fluid}} = 1 \ ,$$

[2] In this study, we will not discuss more advanced viscous forces (Svoboda et al., 1994; Riedel et al., 1994) (including time- and temperature dependencies) because this dissipative force is mainly a means of dissipating surplus energy and not so much based on realistic assumptions about the behavior of the material (Riedel et al., 1994). Also in the limit of the fluid, a more realistic viscous force law would be required, but since we will not reach this limit, we rather prefer to keep the model as simple as possible. Extensions of the present model are always possible in the future.

which, in combination of the two previous equations, leads to the ratio of fluid and solid volumes

$$V_{\text{fluid}}/V_{\text{solid}} = a_{\text{fluid}}^2/a_0^2 = \pi/(2\sqrt{3}) \ .$$

The minimum radius for the incompressible melt is $a_{\text{fluid}} = a_0 - \delta^{\text{fluid}} = a_0\sqrt{V_{\text{fluid}}/V_{\text{solid}}} \approx 0.9523\, a_0$ which corresponds to the maximum overlap

$$\delta^{\text{fluid}} \approx 0.0477\, a_0 \ ,$$

in two dimensions. In the following, we use $\delta^{\text{fluid}}/a_0 = 0.20$ in order to magnify the range of possible non-fluid overlaps.

The stiffness is maximal in the fluid limit for $\delta_0 = \delta^{\text{fluid}}$, which corresponds to $\delta_{\max} = \delta_{\max}^{\text{fluid}} = k_2\delta^{\text{fluid}}/(k_2 - k_1)$, and varies between k_1 and k_2 for smaller overlaps, so that

$$k_2(\delta_{\max}) = \begin{cases} k_2 & \text{if } \delta_{\max} \geq \delta_{\max}^{\text{fluid}} \\ k_1 + (k_2 - k_1)\frac{\delta_{\max}}{\delta_{\max}^{\text{fluid}}} & \text{if } \delta_{\max} < \delta_{\max}^{\text{fluid}} \end{cases} \ . \tag{7}$$

For large overlaps (in the fluid regime), the stiffness and the force is thus only dependent on k_2, independent of k_1. For smaller overlaps both k_1 and k_2 affect the force together with the history of this contact.

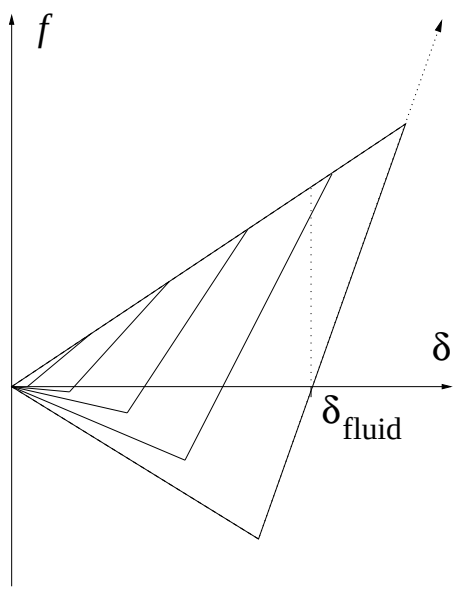

Fig. 3. Force law with varying stiffness $k_2(\delta_{\max})$, according to Eq. (7). If δ_0 becomes larger than δ^{fluid}, the stiffness remains equal to k_2 and the force remains on the corresponding liquid branch with slope k_2 (dotted line). The cohesion strength is maximal for the maximum contact strength and decreases with k_2, see subsection 3.5 for details.

The stiffness in the incompressible fluid should diverge; however, for reasons of numerical stability, we have to limit the maximum stiffness to k_2. Larger stiffness values would require smaller time-steps which would reduce the simulation efficiency. Therefore, the model does not really take the incompressibility of the liquid into account, see Fig. 3. In the fluid no plastic deformation can take place so that δ_0 is fixed and cannot be shifted to larger force free overlaps – in contrast to the hysteretic model described above.

In summary, the hysteretic stiffness model takes into account an increasing stiffness with increasing overlap. The first loading is plastic with low stiffness, and subsequent un- and reloading are stiffer because the material was initially compressed. As a consequence, also the maximum cohesive force depends on the maximum compression which was experienced by the contact during its history. If the material is compressed so strongly that the liquid density is reached, the force-free overlap is equal to the fluid equivalent overlap and the material behaves like a fluid.

3.2 Density Temperature Dependence

If a solid or a liquid (we assume a simple material here - not like water - where the density dependence on the temperature is continuous through the phase transition) is heated, in general, its volume increases so that its density decreases. Therefore, we assume a temperature dependent density of the single particles (disks with radius a and height h):

$$\rho(T) = \frac{m}{\pi a^2 h} = \rho(T_{\text{melt}}) + \delta\rho_T \left(T_{\text{melt}} - T\right) , \tag{8}$$

with the density change per unit temperature $\delta\rho_T$. This corresponds (in linear approximation) to a change of the particle radius

$$a(T) = a(T_{\text{melt}})[1 - \delta a_T \left(T_{\text{melt}} - T\right)] , \tag{9}$$

with the relative change of the radius per unit temperature δa_T. This approximation can be used if the range of temperatures (in Kelvin) is rather narrow and the changes per unit temperature are very small.

In the following, we use $\delta a_T = 10^{-4}\,\mathrm{K}^{-1}$, so that the particle radius is changed by 0.01 per-cent if the temperature is changed by one Kelvin. In the interesting range of temperatures between a low temperature (80^0C) and some melting point (120^0C), the radius changes by one per-cent, accordingly. Note however, that this is an arbitrary choice (reasonable for polyamid); coefficients for steel and glass are typically one and two orders of magnitude smaller, respectively.

3.3 Contact Temperature Dependence

For the temperature dependence, we focus on an inhomogeneous material with a melting temperature T_{melt} and assume that the material behaves statically, as described above, if the temperature T is much smaller than the melting temperature. The behavior of the stiffness k_1 is schematically shown in Fig. 4 as a function of the temperature.

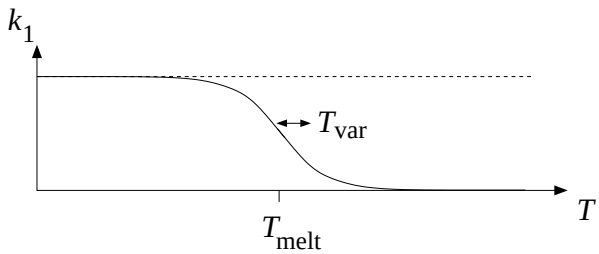

Fig. 4. Schematic plot of the stiffness k_1 as a function of the temperature.

The material becomes softer when $T_{\text{melt}} - T$ becomes small and will lose all stiffness in the limit $T_{\text{melt}} - T \ll 0$. The temperature range in which the melting takes place is quantified by T_{var}. In the transition regime $|T_{\text{melt}} - T| \approx T_{\text{var}}$, the particles are significantly softer than in the *cold* limit $T_{\text{melt}} - T \gg T_{\text{var}}$. In the *hot* and the liquid regime, $T - T_{\text{melt}} \gg T_{\text{var}}$, one has $k_1 \to 0$ and the particles lose their nature. However, the 'incompressibility' is accounted for with a stiffness k_2, as defined in Eq. (7), and $\delta_0 = \delta^{\text{fluid}}$ is fixed.

3.3.1 Increasing temperature

When the temperature is increased to a rather large value, close to the melting point, two particles under stress and in equilibrium due to compressive forces will lose stiffness and thus will deform more strongly so that their overlap becomes larger. Therefore, we assume for the stiffness coefficient

$$\begin{aligned} k_1(T) &= \frac{k_1}{2}\left[1 + \tanh\left(\frac{T_{\text{melt}} - T}{T_{\text{var}}}\right)\right] \\ &= \frac{k_1}{2}\left[1 + \tanh(\tau)\right] \ , \end{aligned} \tag{10}$$

where τ denotes the ratio of the temperature difference to the range of considerable temperature dependency T_{var}, see Fig. 4. If experimentally available in the future, the function $\tanh(x)$ can be replaced by any other function $f(x)$ that decays from unity to zero at $x \approx 0$.

When k_1 is reduced due to an increase in temperature (+), we assume that δ^+_{max} remains constant, so that one obtains a larger force-free overlap $\delta^+_0(T) =$

$[1 - k_1(T)/k_2(\delta^+_{\max})]\delta^+_{\max}$. Thus the material volume shrinks due to sintering at the contact level.

Note that k_2 is not changed directly when $k_1(T)$ is decreased, see the left panel in Fig. 5 or Eq. (7). The cohesion in this model, however, is directly affected by a change of $k_1(T)$, see Eq. (13). In a pre-stressed situation, corresponding to a finite confining force at the contact, also $\delta^+_{\max}$ is shifted in order to balance the confining force – but only after $k_1\delta^+_{\max}$ became smaller than the confining force.

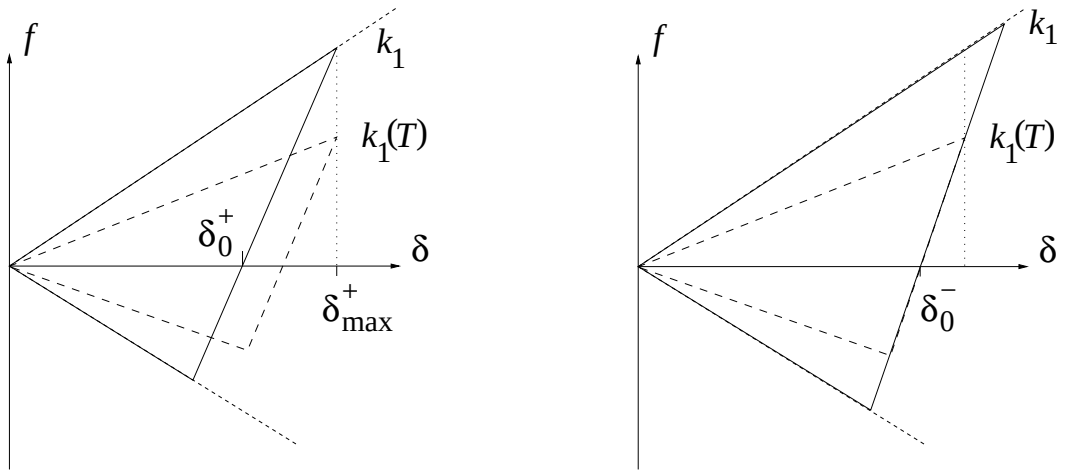

Fig. 5. Force laws for varying stiffness k_1, according to Eq. (10). (Left) If the temperature is increased, k_1 is reduced while $\delta^+_{\max}$ remains constant (dashed line, stress-free case). (Right) If the temperature is subsequently decreased, k_1 is increased while δ^-_0 remains constant (solid line with slope k_2).

If, as an example, the material has a melting point $T_{\text{melt}} = 120^0$C with a range of softening of $T_{\text{var}} = 10^0$C, for a temperature of $T = 118^0$C, the stiffness k_1 is reduced to 0.6 of its cold-limit value, for a temperature of 122^0C the stiffness is 0.4, and for a temperature of 130^0C the stiffness is only 0.12. For a temperature of $T = 160^0$C only a stiffness of 3.10^{-4} remains. The fact that there is a remaining stiffness above the melting temperature can be attributed to the inhomogeneity of the material, i.e. not all the material melts at the same temperature.

3.3.2 Decreasing temperature

If later in time the temperature is decreased again, $k_1(T)$ is adjusted according to Eq. (10), but since the melted (sintered) area around the contact point will not return to its previous state, we now assume that $\delta^-_0 = \text{const.}$, so that the maximum overlap increases to the value $\delta^-_{\max}(T) = \delta^-_0/[1 - k_1(T)/k_2]$, see the right panel in Fig. 5. Therefore, a temperature cycle involving a temperature close to the melting temperature leads to a contact situation similar to the one obtained through some larger maximum compressive force. The contact

deformation/area and thus the force-free overlap become larger due to the partial melting of the surface and also the stiffness is increased accordingly.

The temperature dependence thus can lead to changes of the stiffness and increases the overlap (deformation) of the particles. It is effective only if the temperature is changed – the time dependence will be introduced in the next subsection.

3.4 Temperature dependence with time

In the material there are several time dependent processes taking place. Since we are interested in the long time behavior of the material, we assume that heat conduction and equilibration take place instantaneously, as long as temperature changes are small and slow. The realistic simulation of heat-conduction in the sample is far from the scope of this study. Therefore, the particle size is adjusted directly with the temperature according to Eq. (9).

In addition to the direct effect of a temperature change on the particle size and the stiffness, the material may change its internal, atomistic structure such that defects heal and disappear. This effect will occur mainly in the regime of high temperatures close to the melting point. Therefore, in order to account for such slow microscopic processes, a time dependence is introduced that leads to a change of the material stiffness k_1 with time. The change takes place extremely slowly with an algebraic time dependence, so that $k_1(T,t)$ lags behind when varying from its actual value to the desired, final value $k_1(T)$, as defined in the above equation (10).

When the temperature is increased from a small value T_0 to T, then $k_1(T_0)$ changes to $k_1(T)$ following the law

$$k_1(T,t) = k_1(T)\left[1 - \frac{1}{\frac{1}{1-k_1(T_0)/k_1(T)} - \frac{t}{t_0}}\right] , \tag{11}$$

which corresponds to the rate of change

$$\frac{\partial k_1(T,t)}{\partial t} = \pm\frac{[k_1(T) - k_1(T,t)]^2}{k_1(T)\,t_0} , \tag{12}$$

with the time scale t_0 on which a typical change takes place. Note that k_1, $k_1(T)$, and $k_1(T,t)$ are different, in general, and correspond to the maximum k_1, the temperature dependent $k_1(T) < k_1$, and the time dependent $k_1(T,t)$ that tends towards $k_1(T)$. The sign in Eq. (12) is chosen according to the sign

of $[k_1(T) - k_1(T,t)]$ in Eq. (11) [3].

Assume $T_0 = 20^0$C and $T = 118^0$C, so that $k_1(T_0) = 1$ corresponds to $k_1(T) = 0.6$. The stiffness as a function of time is plotted in Fig. 6 for the time constant $t_0 = 10$s.

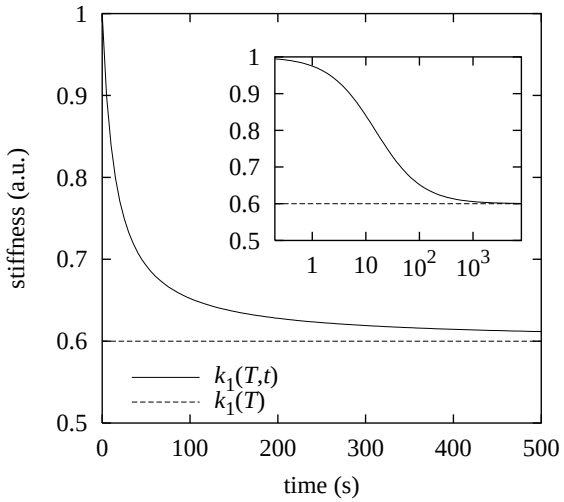

Fig. 6. Variation of the stiffness k_1 with time, see Eq. (11). The inset shows the same function with a logarithmic time axis – only after about 10^3 s the final stiffness is reached.

Note that, due to the factor $k_1(T)$ in the denominator of Eq. (12), the change of stiffness is faster for higher temperatures. In the hot limit, changes take place very rapidly, whereas in the cold limit changes are extremely slow.

Finally, we note that the adaptation/relaxation of $k_1(T,t)$ to the desired $k_1(T)$ value follows the above equations in all cases except when the temperature is going down and the $k_1(T) > k_1(T,t)$. In that situation the contacts freeze rapidly and thus have to become strong as fast as the system cools down.

3.5 Cohesion dependence on stiffness and friction

The cohesive properties of a particle contact depend on the temperature, in so far that a melted contact should have weak tensile and compressive strength. Therefore, we couple the cohesive parameter k_c to the magnitude of $k_1(T,t)$, see Eq. (11), which decreases with temperature increasing. In addition, in order to take into account a reduced tensile strength of a soft contact with weak deformation and thus small overlap, the cohesion is directly related to

[3] In symbolic form this means: $\pm[y]^2 = y|y|$. For the numerical integration, we remark, that the value of the actual stiffness should be $k_1(T, t - \Delta t)$, otherwise we obtained a numerically instable behavior in some situations

the stiffness $k_2(\delta_{\max})$, see Eq. (7). Thus, we propose

$$k_c(T,t,\delta_{\max}) = \frac{k_1(T,t)}{k_1}\frac{k_2(\delta_{\max})}{k_2}k_c \ . \tag{13}$$

This is an arbitrary choice for the cohesive force factor k_c, but as long as no detailed experimental results are available, we stick to this empirical law, see Fig. 3 for a schematic picture.

3.6 Tangential Contact Model

The force in the tangential direction is implemented in the spirit of Cundall and Strack (Cundall and Strack, 1979) who introduced a tangential spring in order to account for static friction and elastic energy stored in the contact tangential direction. Various authors have used this idea and numerous variants were implemented, see (Brendel and Dippel, 1998) for a summary and discussion.

Since we combine cohesion and friction and introduce time and temperature dependencies, it is convenient to repeat the model and define the implementation. First, the tangential force is coupled to the normal force via Coulomb's law, i.e. $f^t \leq \mu f^n$, where for the limit case one has sliding friction and for the case of small forces f^t, one has static Coulomb friction. The latter situation requires an elastic spring in order to allow for a restoring force and a non-zero remaining tangential force in static equilibrium due to activated Coulomb friction. The tangential spring is extended during sticking and is dragged along the contact during sliding.

As a consequence of the cohesion force in the normal direction, attractive forces are possible so that Coulomb's law has to be modified

$$f^t \leq \mu(f^n - f_{\min}) \ , \tag{14}$$

with the minimum (maximum attractive) force

$$f_{\min} = -\frac{k_2(\delta_{\max}) - k_1(T,t)}{1 + k_2(\delta_{\max})/k_c(T,t,\delta_{\max})}\delta_{\max} \ . \tag{15}$$

The equality '=' in Eq. (14) corresponds to (fully) activated, sliding friction, while the inequality '<' corresponds to static friction. Thus the tangential force is related to the normal force relative to the point of cohesion-failure. For normal forces larger than $f_{\min}$, friction is always active and the amplitude is proportional to $f^n - f_{\min}$ and μ. This can lead to a stable equilibrium of the solid also at $f^n \approx 0$ and activated tangential static friction. Note that

$f_{\min}$ tends towards zero for vanishing overlap, so that the difference from the original model also vanishes for vanishing overlap.

If $f^n - f_{\min} > 0$, the tangential force is active, and we project the tangential spring-length $\boldsymbol{\xi}$ into the actual tangential plane by subtracting a possible (small) normal component. This is necessary, since the frame of reference of the contact may have rotated since the last time-step.

$$\boldsymbol{\xi} = \boldsymbol{\xi}' - \boldsymbol{n}(\boldsymbol{n} \cdot \boldsymbol{\xi}') \ . \tag{16}$$

This action is relevant for an already existing spring. If the spring is new, the spring-length and the tangential force are zero anyway; the change of the spring-length is defined below. Next, the relative tangential velocity of the surface of the two particles is computed

$$\boldsymbol{v}_t = \boldsymbol{v}_{ij} - \boldsymbol{n}(\boldsymbol{n} \cdot \boldsymbol{v}_{ij}) \ , \tag{17}$$

with the total relative velocity

$$\boldsymbol{v}_{ij} = \boldsymbol{v}_i - \boldsymbol{v}_j + a_i \boldsymbol{n} \times \boldsymbol{\omega}_i + a_j \boldsymbol{n} \times \boldsymbol{\omega}_j \ . \tag{18}$$

In the next step we calculate the tangential test-force as the sum of the tangential spring- and viscous-force (similar to the normal spring- and viscous-force)

$$\boldsymbol{f}_t^{\mathrm{o}} = -k_t \, \boldsymbol{\xi} - \gamma_t \boldsymbol{v}_t \ , \tag{19}$$

with the tangential spring stiffness $k_t = \alpha k_2(\delta_{\max})$, with a typical stiffness ratio $\alpha = 0.2$, see (Luding, 1998), and the tangential dissipation parameter γ_t. If $|\boldsymbol{f}_t^{\mathrm{o}}| \leq f_C$, with $f_C = \mu(f^n - f_{\min})$, one has static friction and, on the other hand, if $|\boldsymbol{f}_t^{\mathrm{o}}| > f_C$, sliding friction is active. In the former case, the tangential test force is incremented

$$\boldsymbol{\xi}' = \boldsymbol{\xi} + \boldsymbol{v}_t \Delta t_{\mathrm{MD}} \ , \tag{20}$$

to be used in the next iteration in Eq. (16), and the force $\boldsymbol{f}^t = \boldsymbol{f}_t^{\mathrm{o}}$ from Eq. (19) is used. In the latter case, the tangential spring is adjusted to a length which is consistent with Coulomb's condition

$$\boldsymbol{\xi}' = -\frac{1}{k_t} \left(f_C \, \boldsymbol{t} + \gamma_t \boldsymbol{v}_t \right) \ , \tag{21}$$

with the tangential unit vector, $\boldsymbol{t} = \boldsymbol{f}_t^{\mathrm{o}} / |\boldsymbol{f}_t^{\mathrm{o}}|$, defined by the tangential spring, and the Coulomb force is used. Inserting $\boldsymbol{\xi}'$ into Eq. (19) leads to $\boldsymbol{f}^t \approx f_C \boldsymbol{t}$ in the next iteration [4]. In short notation this reads

$$\boldsymbol{f}^t = +\min\left(f_C, |\boldsymbol{f}_t^{\mathrm{o}}|\right) \boldsymbol{t} \ . \tag{22}$$

[4] Note that $\boldsymbol{f}_t^{\mathrm{o}}$ and $\boldsymbol{v}_t$ are not necessarily parallel in three dimensions. However, the mapping in Eq. (21) works always, rotating the new spring such that the direction of the frictional force is unchanged

Note that the tangential force described above is identical to the classical Cundall-Strack spring only in the limit $\gamma_t = 0$ and $k_c = 0$. Besides the combination of the cohesive and the frictional force, also the tangential dissipation is non-standard. Furthermore, we remark that the cohesion could also be coupled to friction in the sense that a broken contact loses its tensile strength when it is assumed brittle, so that $k_c = 0$, (if sliding), i.e. if one has a sliding contact with $f^t = \mu(f^n - f_{\min})$ [5].

3.7 Temperature dependence in tangential direction

In parallel to the change of normal stiffness, the tangential stiffness is always kept in a constant ratio to k_2 so that

$$k_t = \alpha k_2(\delta_{\max}) \ , \tag{23}$$

since the stiffness in the tangential direction is based on the same arguments as the material stiffness in the normal direction.

The friction is coupled to the temperature dependent value of the stiffness $k_1(T,t)$, because friction should not be present in a liquid at large enough temperatures, so that

$$\mu(T,t) = \frac{k_1(T,t)}{k_1}\mu \ . \tag{24}$$

Thus friction is modified together with the changes in normal direction. No new ideas are introduced for the tangential forces.

4 Results

In this section, the sintering model is applied to the sintering process of a particulate material sample. The material is initially a loose powder and first has to be prepared at low temperature from time t_0 to time t_{heat}, see Fig. 7. The preparation takes place with a system as described in section 2 with isotropic external pressure $p := p_{\text{w}} = p_x = p_z = 10$ or 100. The particles are randomly placed in a box with random initial velocity. Then the walls compress the system and motion is dissipated until a quasi-static situation

[5] On the other hand, if the particles are very small, attractive forces could still be present so that k_c would not be affected by the type of the contact being either sliding or sticking. In this study we assume, as an arbitrary, possibly inconsistent choice, $f^n \geq 0$, (if sliding), thus disregarding cohesion in the sliding situation. The effect of this choice has to be examined in more detailed elsewhere.

is reached. Here, we used frictionless particles for the initial compression and thus obtain an over-consolidated initial packing.

Pressure is measured in units of $\mathrm{N\,m^{-1}}$ due to the two-dimensional nature of the model, i.e. p has the same units as the spring stiffness k_2. The correct units of the pressure can be obtained by division through the length of the cylinders (particles). Since the length is rather arbitrary, we drop the unit of pressure in the following for the sake of simplicity. Due to the linearity of the model, some stress σ can be rescaled/non-dimensionalized with the spring stiffness k_2 and has thus to be read as the dimensionless quantity $p = p_0\sigma/k_2$, with $p_0 = 2.10^5$. When, for example, a wall pressure $p = 100$ occurs below in the paper, this can be translated to a stress $\sigma = k_2 p/p_0$. However, a detailed study of the scaling behavior of the stresses is far from the scope of this study.

Note that the pressure is therefore related to the typical overlap of two particles: A pressure of $p = 100$ corresponds to $100 = 2.10^5 p/k_2 = 2.10^5 f^n/(2ak_2) = 2.10^5(\delta - \delta_0)/(2a)$ or $(\delta - \delta_0)/a \approx 10^{-3}$, while $p = 10$ corresponds to approximately $(\delta - \delta_0)/a \approx 10^{-4}$. This can also be interpreted as mean normal force $f^n \approx 2ap$. However, these are rough estimates only, since the contact forces and the overlaps are strongly varying in magnitude for one situation, as will be discussed in more detail below.

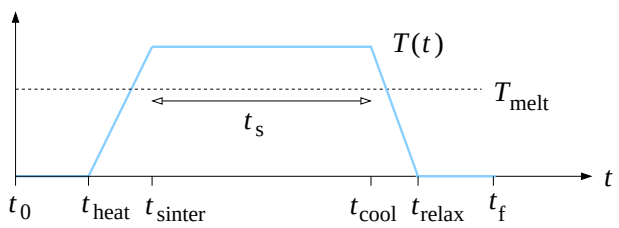

Fig. 7. Schematic plot of the temperature variation during simulation.

The other system parameters are summarized in table 1, where multiple numbers mean that a series with the corresponding values was performed.

4.1 Sample preparation

The preparation of the sample consists of an initial relaxation period at constant temperature $T = 80^0$C until time t_{heat}, when the system is heated up to $T = 140^0$C between time t_{heat} and t_{sinter}. During the sintering time t_s, the system is allowed to sinter with a much shorter relaxation time $t_0 = 0.1$. This 'trick' allows for a long time sintering simulation while keeping the simulation time small. During sintering, the time axis should be stretched by a factor of 10^4 in order to obtain the real-time behavior. At the end of the sintering process, at time t_{cool}, the sample is slowly cooled down and, at time t_{relax} allowed to relax at constant temperature until time t_{f}. With this finished sample, tests

	particle numbers N	100, 300
	mean particle radius a_0	1 mm
	relative width of size distribution w_0	± 0.5
	particle height h	6 mm
	particle density ρ_p	$2000\,\mathrm{kg\,m^{-3}}$
	particle stiffness k_2	$2.10^5\,\mathrm{N\,m^{-1}}$
	particle stiffness k_1/k_2	0.5
	particle stiffness k_c/k_2	0.5
	particle stiffness k_t/k_2	0.2
	particle normal damping γ_0	$0.2\,\mathrm{kg\,s^{-1}}$
p	particle tangential damping γ_t	$0.05\,\mathrm{kg\,s^{-1}}$
	particle-particle friction μ	0.5
	particle-wall friction μ_w	0
	melting temperature T_{melt}	120^0C
	temperature variation T_{var}	10 K
	density variation with temperature δa_T	$10^{-4}\,K^{-1}$
	fluid overlap δ^{fluid}	0.2
	relaxation time t_0 (default)	10^3 s
	relaxation time during sintering	10^{-1} s
	wall mass m_{w}	0.01
	wall damping γ_{w}	0.2

Table 1
Summary of the system properties and material parameters as used in the simulations

will be performed later, but first we discuss the preparation process.

For the preparation of the sample, we use the times $t_0 = 0$, $t_{\mathrm{heat}} = 0.2$, $t_{\mathrm{sinter}} - t_{\mathrm{heat}} = 0.1$, different sintering times $t_s := t_{\mathrm{cool}} - t_{\mathrm{sinter}}$, $t_{\mathrm{relax}} - t_{\mathrm{cool}} = 0.1$, and $t_{\mathrm{f}} - t_{\mathrm{relax}} = 0.1$. Note that the time unit is arbitrary, since a slower preparation procedure did not lead to notably different results, i.e. the process takes place in the quasi-static limit. Only the long-time sintering is affected by a change of the relaxation time t_0.

4.1.1 Temperature and stiffness

The variation of $k_1(T,t)$ with time is plotted in Fig. 8, where the algebraic, slow decay of the stiffness with time becomes evident. The number of particles was $N = 300$, the sidestress $p = 100$, and the other parameters are given in table 1.

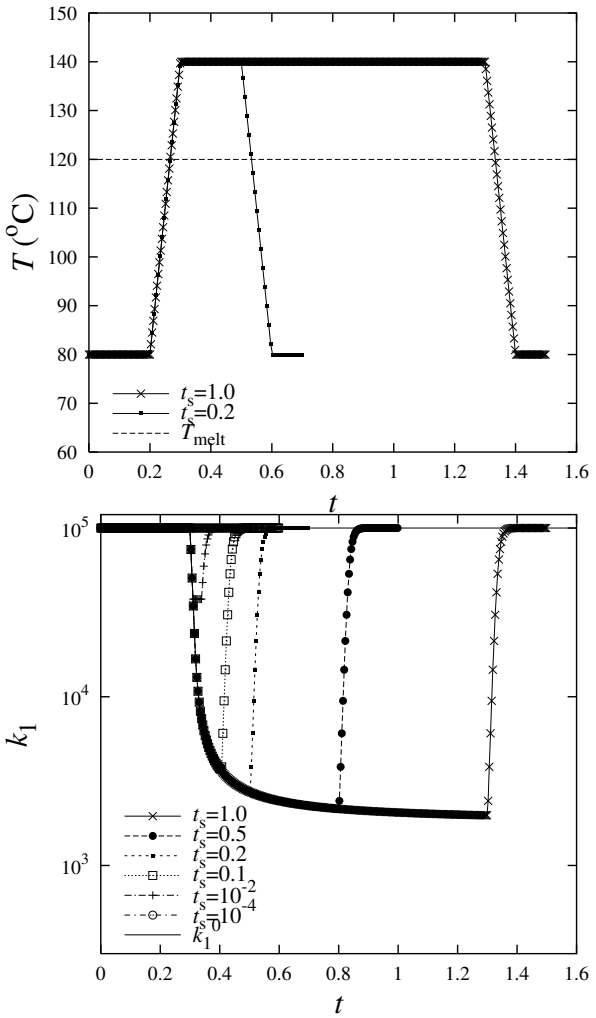

Fig. 8. (Top) Temperature during the preparation procedure and (bottom) material stiffness $k_1(T,t)$ as function of time for 'experiments' with different sintering times t_s.

4.1.2 Density

The longer the sintering time t_s, the lower the value of k_1 gets. For short sintering time, the lowest values are never reached, because the system is cooled down before the sintering is finished. At the end of the sintering time, k_1 is increasing during the cooling process of the sample and reaches its inital value. However, the melting and sintering of the contacts is *not reversed*, as becomes evident when plotting the volume fraction ν in Fig. 9.

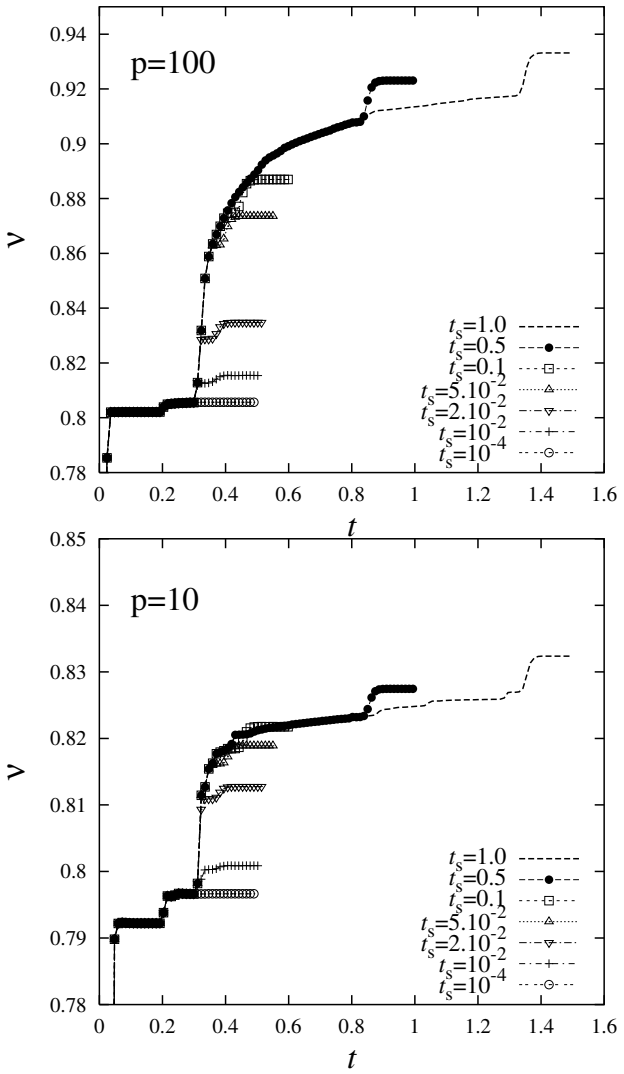

Fig. 9. Material density ν as function of time for simulations with $N = 300$ particles and side stress $p = 100$ (top) and $p = 10$ (bottom). Note the different vertical axis scaling.

The initial preparation step leads to a rather low density of $\nu \approx 0.8$. At time t_{heat}, the relaxed sample is heated up and, at the same time, the wall friction is switched off. The latter has an immediate effect, a slight increase in density is possible due to reorganizations. The increased temperature only becomes effective at time t_{sinter}, when the relaxation time t_0 is decreased in order to accelerate the evolution of the system. Note that the increase in density due to the sintering seemingly appears quite rapid – due to the quenched time axis during sintering. Up to the beginning of the sintering process all densities are equal due to an identical preparation of the sample. For increasing duration of sintering, t_s, the density successivly increases with t_s. This effect is strongest at the beginning, but continues also for longer times. Below, we will discuss different reasons for this increase in density in more detail. At the end of the sintering process, the system is cooled down, corresponding to the final, small

increase in density, and then relaxes to the final configuration.

4.1.3 Special cases

As a control simulation, also three particles were simulated and sintered in the same way as the larger samples with $N = 100$ and $N = 300$ above. A sample with only three particles has almost no possibility for a rearrangement after the initial load is applied (actually, the three particles were either arranged on a triangle or on a line and did not change their configuration for the cases observed). This artificial test-case shows that the strong increase in density observed for larger samples is caused by re-arrangements of the packing and is not only due to the force model. More quantitatively, the sintering process leads to a densification of about 5% and 16% for $p = 10$ and $p = 100$, respectively, whereas the densification due to the contact law, without rearrangements of the packing, can be estimated to the respective magnitudes of about 0.2% and 8% (data not shown here). Thus, for low confining pressure, reorganizations are much more important than in the case of large external pressure – at least for the parameters used here. In this spirit, network-models or DEM simulations with fixed, e.g. periodic arrangements can not account for large scale reorganization of a packing, which are of eminent importance during the sintering process. Examples for DEM simulations can be found, for example, in (DeLo et al., 1999; Heyliger and McMeeking, 2001; Redanz and Fleck, 2001).

Another control simulation without thermal expansion of the particles, $\delta a_T = 0$, gave no new insights and did not change the outcome of the simulations after cool-down, even though the values of the density were slightly different from the values obtained with a thermal expansion. Therefore, we conclude that the qualitative results are not dependent on detailed parameter values and the sintering behavior, macroscopic as well as microscopic, is generic within the framework of this model.

4.1.4 Summary

In summary, we obtain that longer sintering and larger confining pressures lead to higher densities of the sintered sample. As an example, after the end of the longest sintering process (dashed lines in Fig. 9) at $t = 1.3$, a density of almost 0.92 is reached for $p = 100$. Only after cool-down, the maximum density of almost 0.94 is reached due to negative thermal expansion.

Through test simulations with different parameters, we verified that the increase in density is only partially due to the contact model, but also is caused by reorganizations in the sample. The thermal expansion of the particles, on the other hand, does not affect the results in a drastic way.

In order to understand the behavior of the material during sintering, we take a look at some microscopic quantities of the system, like the coordination number, in Fig. 10.

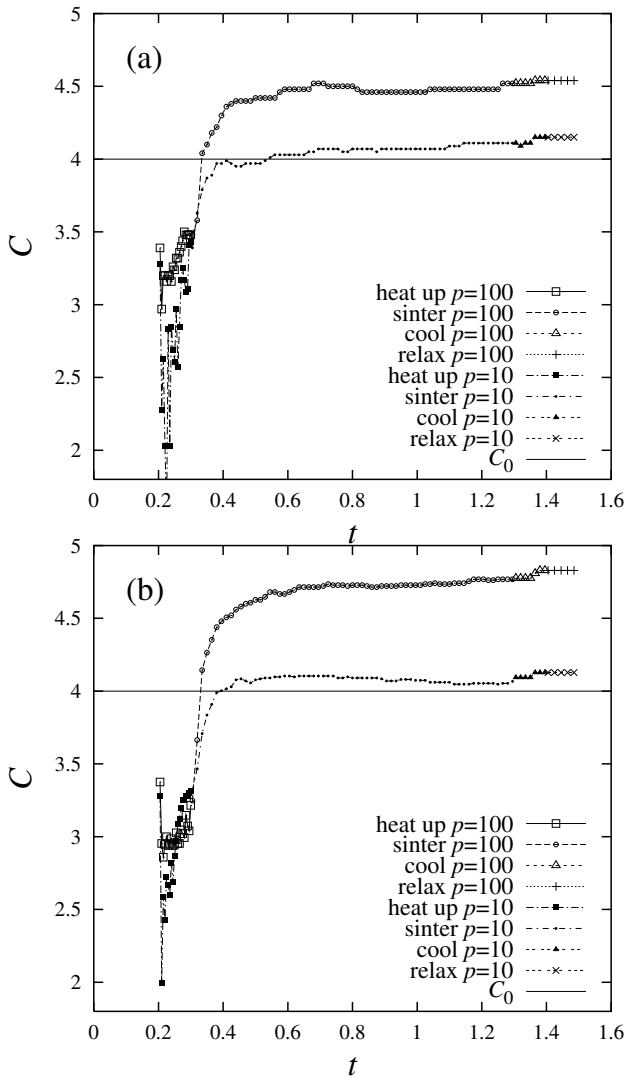

Fig. 10. Coordination number as function of time during the preparation and sintering ($t_s = 1\,\mathrm{s}$) of the sample. Compared are samples of different size, $N = 100$ (a) and $N = 300$ (b), and with different confining stress p.

We note two major issues: First, the larger confining stress, $p = 100$, leads to a larger number of contacts per particle, whereas the samples with small confining stress, $p = 10$, approach a coordination number of $C_0 \approx 4$, as can be expected for a frictionless, isostatic arrangement of disks. Second, the coordination number sometimes decays, whereas the density continuously increases. We attribute this to the fact that, inside the sample, reorganizations can take place, which save space and thus increase the density, but at the same time

can lead to a smaller C.

In order to deepen this insight, the coordination number, the density and the measured wall-stress σ_{zz}/p are plotted in Fig. 11. The continuous increase in density is sometimes accompanied by a decrease of the coordination number and large stress fluctuations. Large scale re-organizations of the packing thus may be responsible for a detectable fluctuation of the stress at the boundaries of the sample, possibly connected to sound emission.

We attribute the difference in C for different particle numbers to the fact that the smaller sample has proportionally more wall contacts, and a particle with a wall contact has typically, on average, less contacts that a particle in the bulk. Therefore, the smaller sample has a somewhat smaller number of contacts (4.5) than the large sample (4.8).

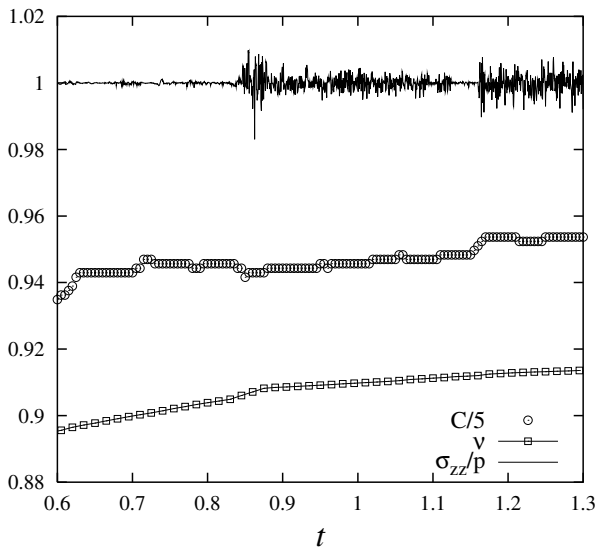

Fig. 11. Density (squares), coordination number (circles), and normalized stress on the top-wall (line), as function of time during the sintering ($t_s = 1\,\mathrm{s}$) of the sample. The coordination number C is divided by a factor, $C/5$, in order to allow a comparison with the other quantities.

4.3 Contact statistics

4.3.1 Compression/deformation/overlap probabilities

A very specific microscopic property of the sintered sample is the statistics of the contacts, i.e. the probability distribution function (pdf) to find a certain overlap δ. After the initial preparation of the powder sample at low temperature, the probability for larger overlaps decays rapidly – no large deformations have taken place.

The overlap probabilities at the final stage of the sintering process are plotted

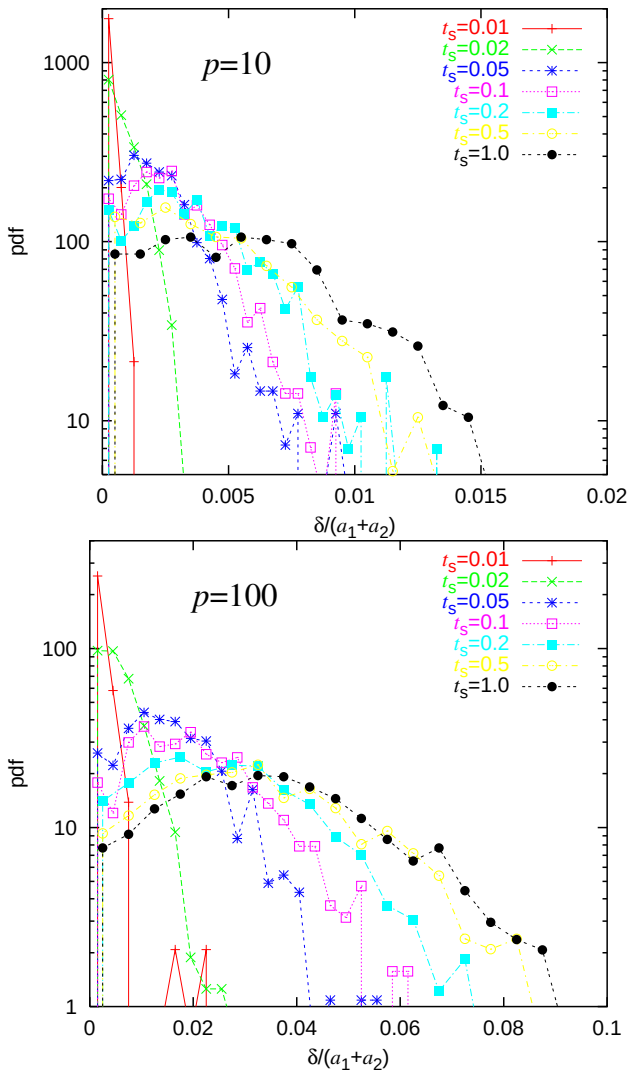

Fig. 12. Overlap probability for overlaps, rescaled with the sum of the radii a_1 and a_2 of the contacting particles, after different sintering durations. The data are taken from the simulations with $N = 300$ at different confining pressure p.

in Fig. 12 for $N = 300$, and both side pressures $p = 10$ and $p = 100$. The probability distributions show many contacts with small overlaps and a rapidly decaying probability for large overlaps at short sintering times. The mean overlap increases, as expected, with the side stress and the sintering time. The larger side stress leads to an underpopulation of small overlaps, because *all* particles are compressed quite strongly.

The probability distributions after the cool-down and the subsequent relaxation are plotted in Fig. 13 for the same simulations. The remarkable difference is not the width of the distribution – that is only slightly wider. The most striking difference is the shape, showing that after cool-down contacts with small overlap are rarefied, while contacts with a typical overlap are overpopulated as compared to the situation before cool-down. The probability for the largest

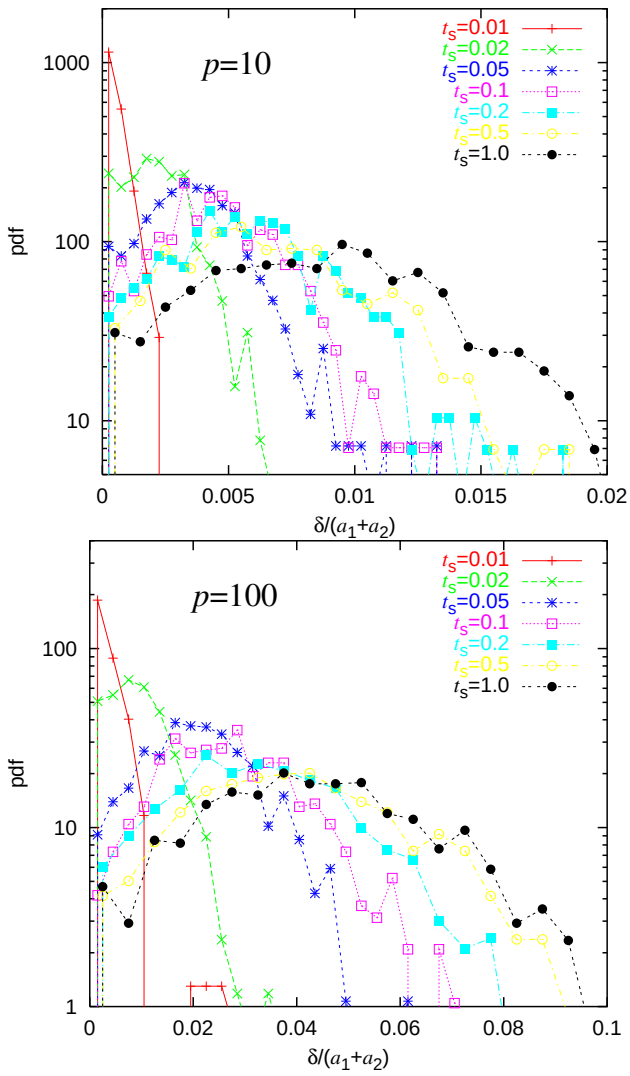

Fig. 13. Overlap probability for overlaps, rescaled with the sum of the radii a_1 and a_2 of the contacting particles, after different sintering durations. The data are taken from the simulations with $N = 300$ at different confining pressure p.

overlaps is still decreasing rapidly.

4.3.2 Normal contact force probabilities

Due to the advanced contact force law, as introduced and used in this study, it is not possible to directly obtain the contact force from the overlap. Therefore, the pdf for the normal contact forces is plotted in Figs. 14 and 15 for small and large side-stresses $p = 10$ and $p = 100$, respectively, and for different sintering times, t_s as given in the inset.

Comparing the pdf for the two situations, after sintering and after cool-down, the astonishing outcome of the simulation is the fact that the contact forces are mostly repulsive and rather small in the hot situation, just before cool-down.

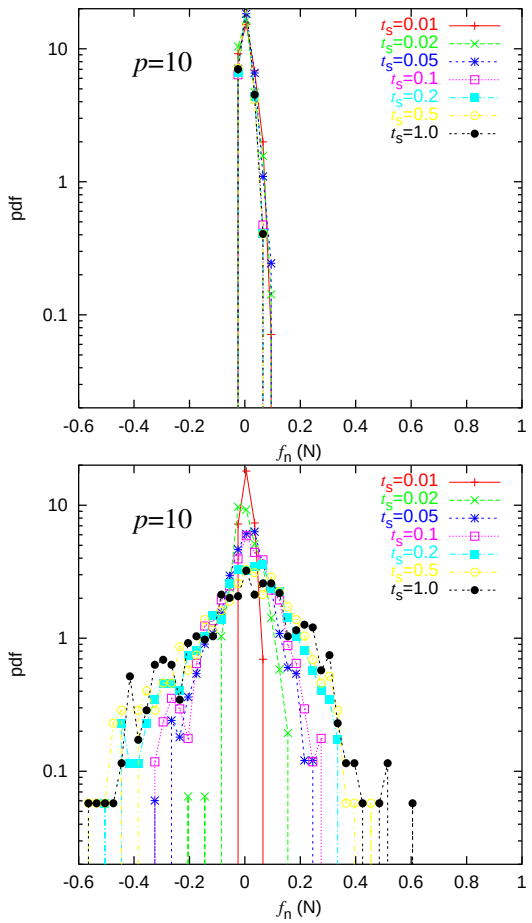

Fig. 14. Contact force probability distribution after the sintering (top) and after the cool-down and relaxation (bottom), for $N = 300$ and $p = 10$.

This situation changes during cooling down: The cooling goes ahead with a broadening of the distribution towards both positive and negative forces. This qualitative result is independent of the side pressure; however, the width of the distribution increases with increasing side stress and increasing sintering time.

Another interesing and unexpected result is the observation that the force distribution *becomes narrower* with sintering. In other words, the extremely large forces are "destroyed" due to long time sintering and the distribution becomes more homogeneous in the sense that its width becomes smaller, see top panel in Fig. 15.

4.3.3 Tangential forces

From the tangential force distribution (data not shown), there are less clear observations to be made. The force distribution shows that during sintering the tangential forces become weaker – as can be expected from the force model, see Eq. (24), since $k_1(T, t)$ decays with increasing temperature and

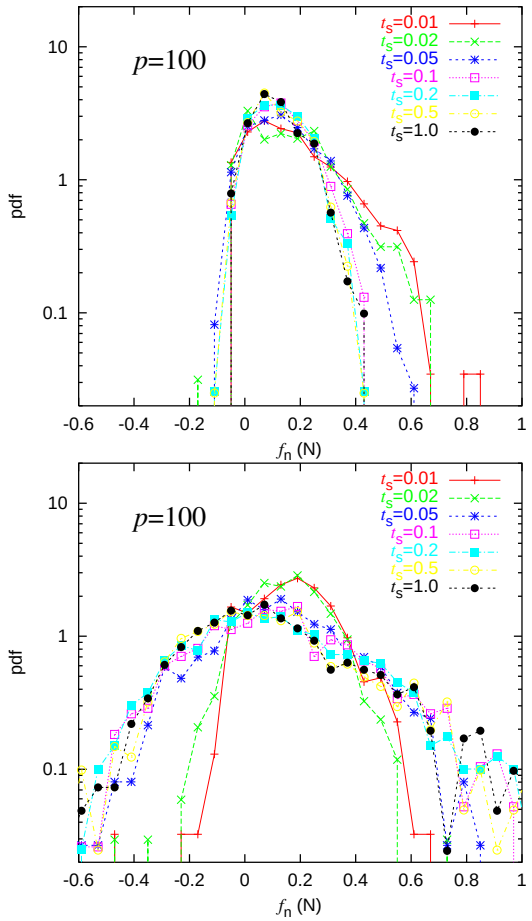

Fig. 15. Contact force probability distribution after the sintering (top) and after the cool-down and relaxation (bottom), for $N = 300$ and $p = 100$.

time. Thus longer sintering leads to weaker tangential forces. However, after cool-down, the tangential force distribution is almost independent of the side stress and the sintering time, if both are sufficiently large. With other words, only for very small side stresses and sintering times, the tangential forces are weakly activated, for larger p or t_s, the tangential forces reach a saturation distribution that is decaying almost exponentially for large f_t.

The second possibility to look at the tangential forces is to measure the amount of friction that is activated, namely $\mu_t := f_t/(f_n - f_{\min})$. This quantity should not become larger than $\mu(T, t)$, as is consistently observed from the data. Contacts where $\mu_t \approx \mu(T, t)$ are referred to as contacts with fully activated friction. These become less probable for longer sintering times since, as mentioned before, the attractive forces become stronger after long sintering and the cooling down. Larger attractive forces correspond to a larger magnitude of $f_{\min}$, so that μ_t becomes smaller.

4.4 Material properties

The samples prepared via the procedure described above are now tested via two test experiments, a compression test, where the vertical confining pressure is slowly increased, and a vibration test, where the confining stress is removed, and the sample is vibrated vertically on a flat bottom. The compression test is performed for two sample sizes, namely with $N = 100$ and $N = 300$, in order to judge the effect of a rather small particle number on the outcome of the simulations. In order to decide about size-independent results or size-effects, more systematic simulations with larger particle numbers are desirable, but are far from the scope of this study.

4.4.1 Compression test (100 particles)

The compression test is a variant of the bi-axial compression frequently used in soil- or powder mechanics. A given compressive stress in one direction ($p = \sigma_{xx}$) is kept constant by moving the right, vertical wall, if neccessary. The other confining stress σ_{zz} is increased by moving the vertical wall down in a defined way – see also section 2. This vertical motion is thus strain controlled, where the vertical strain is defined as $\epsilon_{zz}(t) = 1 - z(t)/z_0$, with the vertical position of the top wall $z(t)$ and $z_0 = z(0)$. Note that a compressive vertical strain is defined positive for convenience here.

For the compression test, the previously prepared samples are used and the top wall is displaced slowly with the vertical strain $\epsilon_{zz}(t)$. The density of a sample with $N = 100$ particles is plotted against the strain for various sintering times and for the two pressures $p = 10$ and $p = 100$ in Fig. 16. The results show again that samples which sintered longer have a higher density. Furthermore, the compressive pressure also affects the sample density in magnitude and also in the variation, i.e. the higher compressive pressure leads to higher densities and also to a broader variation in densities between.

During compression, the density slightly increases first and then decreases strongly. The former is due to compression, the latter is due to dilatancy that is neccessary for the material to shear. The longer the sample was sintered, the stronger is the change in density. We relate this to the existence of the attractive contact forces. For longer sintering, stronger attraction is activated, holding together parts of the sample, so that the compression test leads to fragements with increasing size for increasing sintering duration. For the shortest sintering, the density change due to compression is negligible and the sample fragments into single grains.

The behavior of the material, as for instance its stiffness, is better described in terms of the vertical stress that the material can sustain under load, as

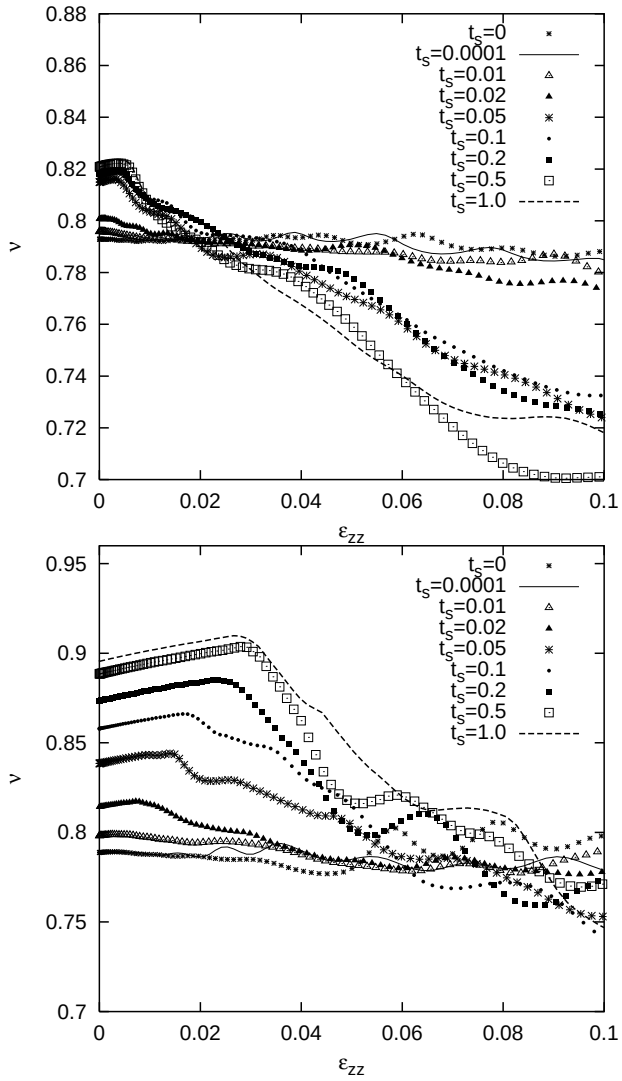

Fig. 16. Material density as function of the vertical strain for samples prepared with different sintering times t_s and different pressure $p_{\mathrm{w}} = 10$ (Top) and $p_{\mathrm{w}} = 100$ (Bottom).

plotted in Fig. 17. The vertical stress in the sample increases and the material fails typically at some failure-strain and at some magnitude of vertical stress: Both the failure-strain and the failure-stress increase with increasing sintering time and increasing external stress. The material stiffness (the slope in this representation) is increased by a factor of about two when the confining stress is increased by a factor of ten. Moreover, the critical strain where the material fails increases with increasing confining pressure. Finally, a rather large jump in material strength is observed for sintering times between $t_s = 0.02$ and 0.05 for the small pressure, not paralleled by a similar outcome for the large stress. Thus the combination of sintering time, compressive pressure and test mode appears quite non-linear and not straightforward.

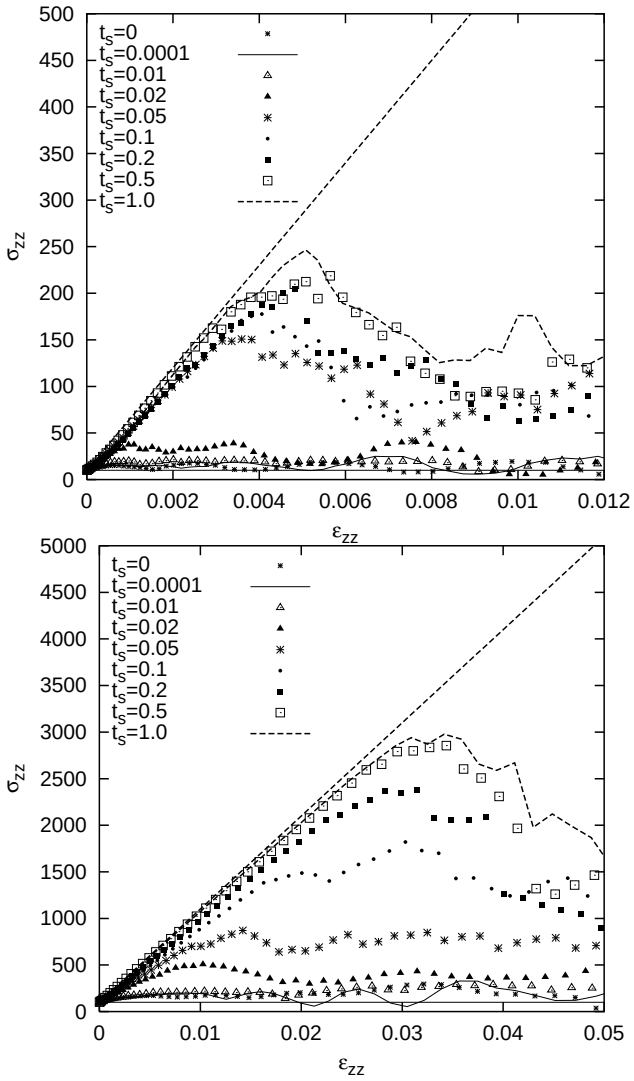

Fig. 17. Vertical stress as function of the vertical strain for samples prepared with different sintering times t_s and different pressure $p_{\mathrm{w}} = 10$ (Top) and $p_{\mathrm{w}} = 100$ (Bottom). The slope of the dashed line (material stiffness) is about double for the higher pressure.

4.4.2 Compression test (300 particles)

For the compression test of the larger samples, also the prepared samples are used and the top wall is displaced slowly with the vertical strain. The density of a sample with $N = 300$ particles is plotted against the strain for various sintering times and for the two pressures p in Fig. 18. The results are qualitatively similar to those obtained for $N = 100$, only the larger sample shows somewhat larger densities that can be attributed to the larger fraction of wall particles in the small sample.

The vertical stress is plotted against the strain in Fig. 19. With increasing strain, the vertical stress in the sample increases and it fails typically at some slightly larger strain and stress as compared with the small sample. The failure

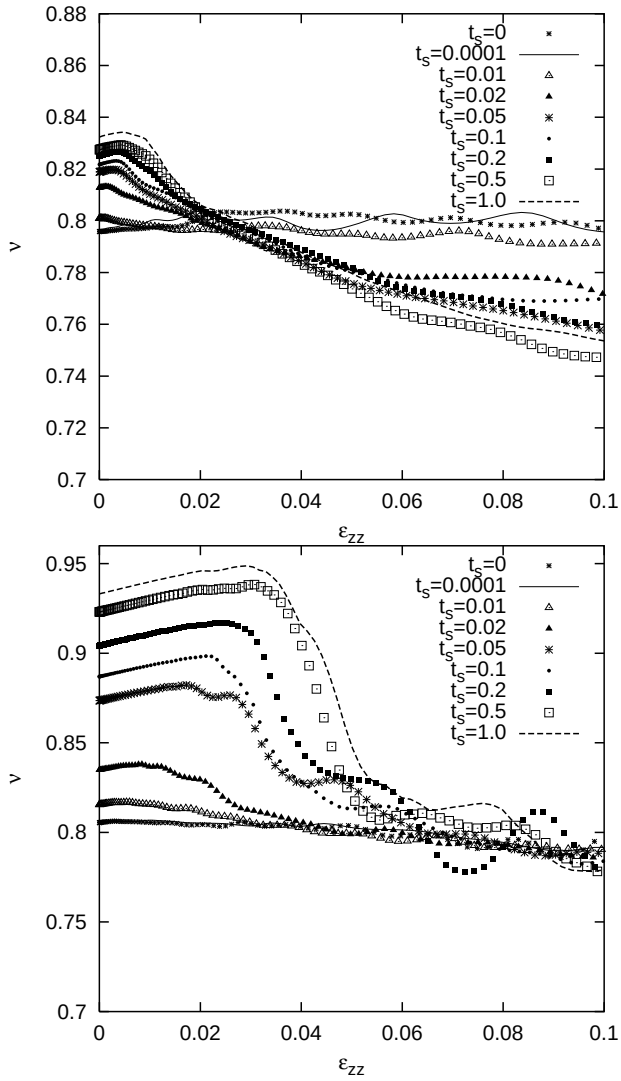

Fig. 18. Material density as function of the vertical strain for samples prepared with different sintering times t_s and different pressure $p_{\mathrm{w}} = 10$ (Top) and $p_{\mathrm{w}} = 100$ (Bottom).

stress increases with increasing sintering time, increasing external stress, and increasing sample size. However, the latter observation is not clearly a size-effect, since the sample size is so small that a non-negligible fraction of the particles is in contact with the walls and thus leads to a different outcome. The material stiffness (dashed line in Fig. 19) is again increased by about a factor of two when the confining stress is increased by a factor of ten. Moreover, the critical strain where the material fails increases with increasing confining pressure, sintering time and system size.

4.4.3 Compression test snapshots

One compression test for a long sintering time, $N = 300$ and $p = 10$ is presented in Fig. 20. During compression (from top to bottom), the lines of

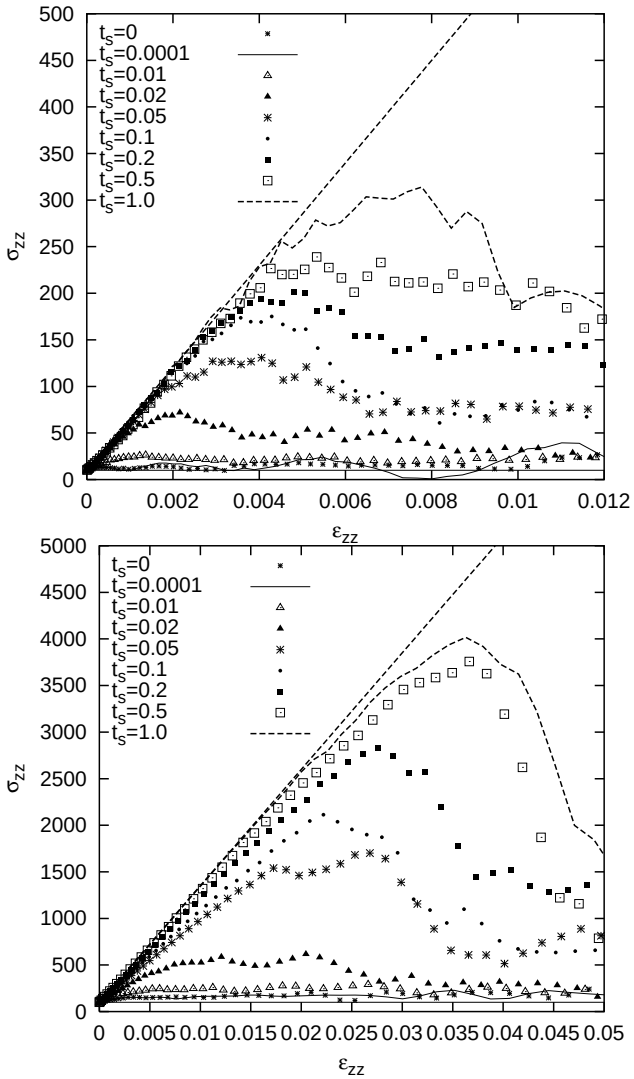

Fig. 19. Vertical stress as function of the vertical strain for samples prepared with different sintering times t_s and different pressure $p_{\mathrm{w}} = 10$ (Top) and $p_{\mathrm{w}} = 100$ (Bottom). The slope of the dashed line (material stiffness) is about double for the higher pressure.

strong attraction (so to say the backbone of the sample) are destroyed and, at the same time, more and more frictional contacts occur due to local shear. Moreover, gaps between the parts of the sample open and it fragments into pieces.

This is only a representative example for the compression test; a more detailed study of the fracture behavior, sample-size- and sintering-time-dependence is far from the scope of this study.

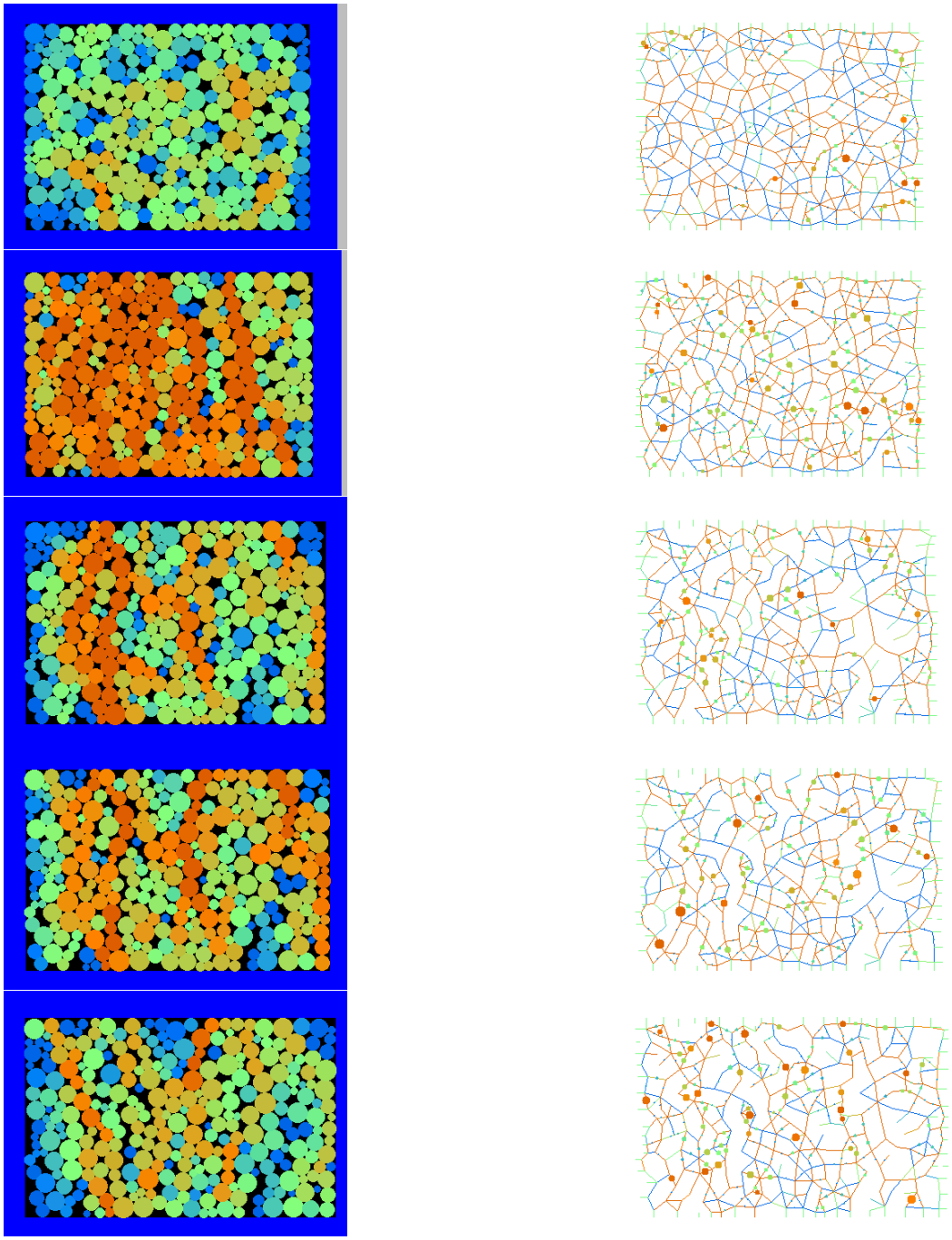

Fig. 20. Snapshots of the compression test with $N = 300$ and $p = 10$. at times $t = 0.005$, 0.02, 0.03, 0.035, and 0.04 (from top to bottom); the material sample was sintered for $t_s = 1.0$. The blue bars are the walls, the circles are the particles with their colors coding the average stress, blue, green and red correspond to low, medium and large stresses. The lines are the contacts with their colors coding attractive (blue) or repulsive (red) normal forces. The small solid circles denote the tangential forces, with their size proportional to the magnitude of the tangential force.

4.5 Vibration test

The sintered samples can also be vibrated (in the gravitational field) in order to probe their stability. The results of the previous tests are paralleled by a vibration test, see Figs. 21 and 22.

Short sintering times lead to unstable material samples, whereas the sample becomes more and more stable with increasing sintering time and confining pressure. The sample with the longest sintering time $t_s = 1.0$ is almost perfectly stable even under strong shaking – some corner- or boundary particles sometimes break off. For shorter sintering time the sample is less stable and fragments into pieces. For very short sintering time, the sample consists of single particles only.

5 Conclusion

In summary, a discrete model for the sintering of particulate materials was introduced and simple material samples were sintered for different times and confining pressures. Then they were tested with respect to their anisotropic load strength: Longer sintering and stronger confining pressure systematically increases the density and the strength of the material. Depending on the sintering duration, either isolated particles, fragments or a single solid block of material could be produced.

Besides this macroscopic point of view, also the microscopic picture was examined. The series of astonishing observations includes: (i) The coordination number may slightly decrease due to reorganizations while the density monotonously increases. (ii) Sintering leads to a broadening overlap distribution, but to a narrowing force distributon, and thus to a homogenization of the sample. (iii) The normal forces become strongly attractive during the cooling down of the sample below the melting temperature. Besides these facts, a lot of open questions concerning the sintering process remain, especially concerning the connection between the microscopic contact-model parameters and the macroscopic material parameters.

The research to be done is an accurate testing of the model via a comparison with experimental data. Since these are only available in three-dimensional systems, the 2D model presented here may be not helpful. (This is why we restricted our efforts to rather small particle numbers, so that we could not judge size-independence or size-effects.) The model can easily be extended to three dimensions, where "only" more particles are needed. Note that the model presented here increases the amount of computation necessary for each

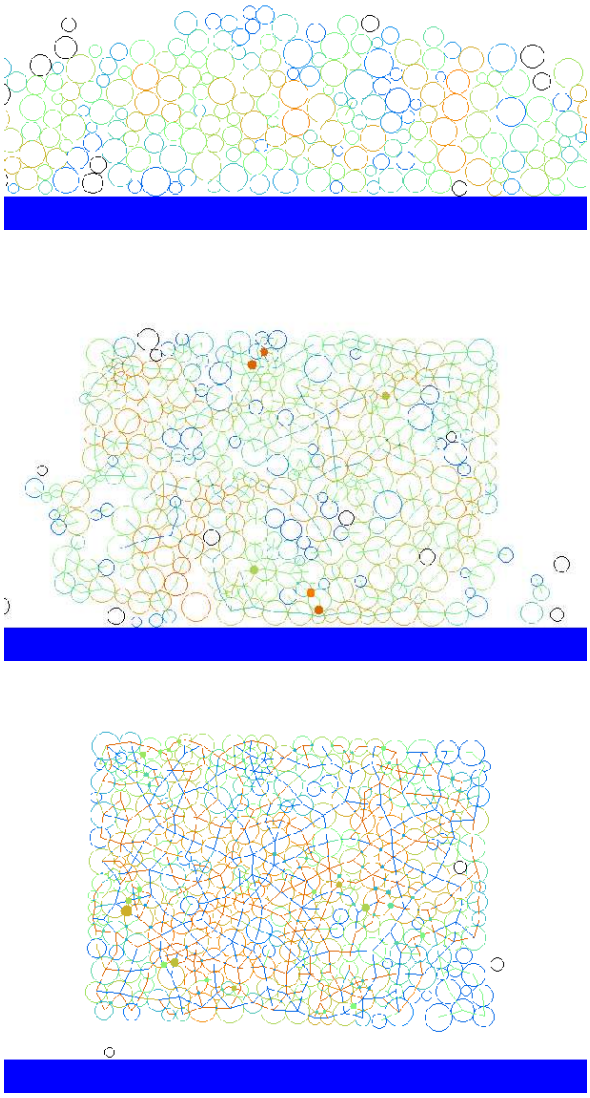

Fig. 21. Snapshots after a vibration test of $t = 0.1$, with frequency $f = 100\,\mathrm{Hz}$ and amplitude $a = 0.2\,\mathrm{mm}$. The material sample was sintered (from top to bottom) for $t_s = 10^{-4}$, 0.02, and 1.0 with $p = 10$. The open circles are particles with their colors coding the average stress, blue, green and red correspond to low, medium and large stresses. The lines are the contacts with their colors coding attractive (blue) or repulsive (red) normal forces. The small solid circles denote the tangential forces, with their size proportional to the magnitude of the tangential force.

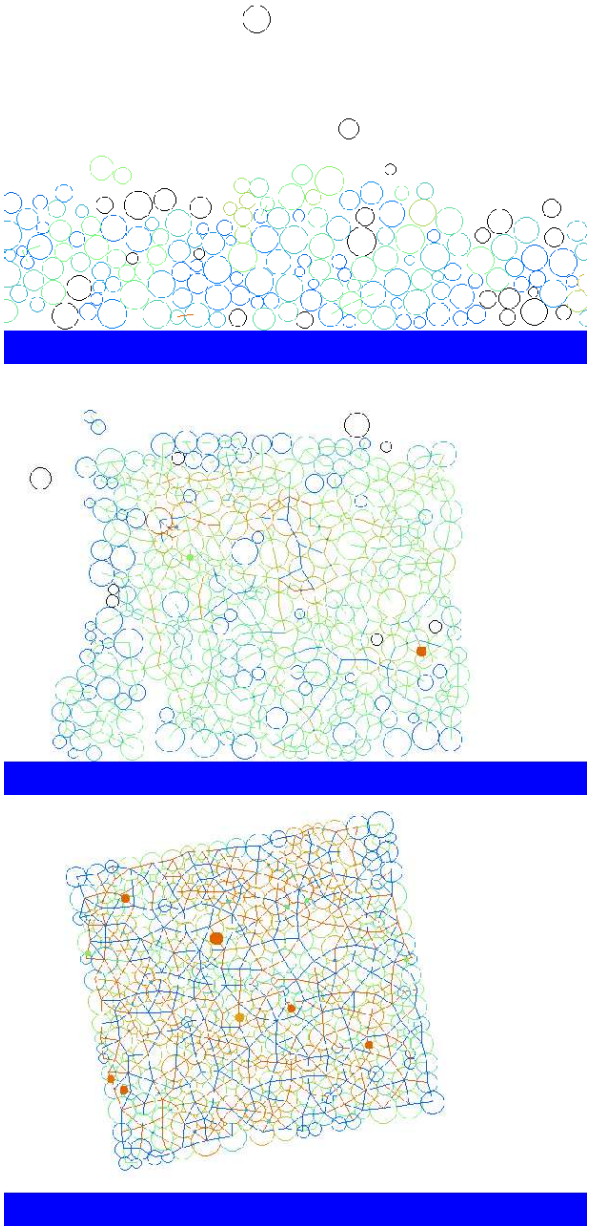

Fig. 22. Snapshots after a vibration test of $t = 0.1$, with frequency $f = 100\,\mathrm{Hz}$ and amplitude $a = 0.2\,\mathrm{mm}$. The material sample was sintered (from top to bottom) for $t_s = 10^{-4}$, 0.01, and 1.0 with $p = 100$. The color coding and figure meaning is the same as in Fig. 21.

contact by a large factor, so that the number of particles possible to simulate becomes rather small for a standard computer. Thus an extension to three dimensions requires a proper tuning of the implementation of the force-model and possibly the view of particles as blocks of material that cannot fragment, rather than isolated particles. The last missing ingredient in the model is a rolling resistance which accounts for a torque resistance of the contacts.

6 Acknowledgements

The authors thank M. Lätzel, J. Tomas, S. Diebels, H. Besserer, and G. A. D´Addetta for discussions and acknowledge financial support by the Deutsche Forschungsgemeinschaft (DFG) and by the DaimlerChrysler research division.

References

Allen, M. P. and Tildesley, D. J. (1987). *Computer Simulation of Liquids*. Oxford University Press, Oxford.

Anestiev, L. A. and Froyen, L. (1999). Model of the primary rearrangement process at liquid phase sintering and selective laser sintering due to biparticle interactions. *J. Appl. Phys.*, 86(7):4008–4017.

Bashir, Y. M. and Goddard, J. D. (1991). A novel simulation method for the quasi-static mechanics of granular assemblages. *J. Rheol.*, 35(5):849–885.

Bellehumeur, C. T., Kontopoulou, M., and Vlachopoulos, J. (1998). The role of viscoelasticity in polymer sintering. *Rheol. Acta*, 37:270–278.

Brendel, L. and Dippel, S. (1998). Lasting contacts in molecular dynamics simulations. In Herrmann, H. J., Hovi, J.-P., and Luding, S., editors, *Physics of Dry Granular Media*, page 313, Dordrecht. Kluwer Academic Publishers.

Cundall, P. A. and Strack, O. D. L. (1979). A discrete numerical model for granular assemblies. *Géotechnique*, 29(1):47–65.

DeLo, D. P., Dutton, R. E., and Semiatin, S. L. (1999). A comparison of discrete element model prediction to observation of metal powder consolidation. *Scripta Materialia*, 40(10):1103–1109.

Herrmann, H. J., Hovi, J.-P., and Luding, S., editors (1998). *Physics of dry granular media - NATO ASI Series E 350*, Dordrecht. Kluwer Academic Publishers.

Heyliger, P. R. and McMeeking, R. M. (2001). Cold plastic compaction of powders by a network model. *Journal of the Mechanics and Physics of Solids*, 49:2031–2054.

Jagota, A. and Dawson, P. R. (1990). Simulation of the viscous sintering of 2 particles. *Journal of the American Ceramic Society*, 73(1):173–177.

Jagota, A., Mikeska, K. R., and Bordia, R. K. (1990). Isotropic constitutive model for sintering particle packings. *Journal of the American Ceramic Society*, 73(8):2266–2273.

Jagota, A. and Scherer, G. W. (1995). Viscosities and sintering rates of composite packings of spheres. *Journal of the American Ceramic Society*, 78(3):521–528.

Kraft, T., Riedel, H., and Rosenfelder, O. (2003). Compaction and sintering of a ceramic seal: Modeling and experimental response. *Int. J. of Powder Metallurgy*, 39(6):27–34.

Luding, S. (1998). Collisions & contacts between two particles. In Herrmann, H. J., Hovi, J.-P., and Luding, S., editors, *Physics of dry granular media - NATO ASI Series E350*, page 285, Dordrecht. Kluwer Academic Publishers.

Luding, S. and Herrmann, H. J. (2001). Micro-macro transition for cohesive granular media. in: Bericht Nr. II-7, Inst. für Mechanik, Universität Stuttgart, S. Diebels (Ed.).

Luding, S., Lätzel, M., and Herrmann, H. J. (2001). From discrete element simulations towards a continuum description of particulate solids. In Levy, A. and Kalman, H., editors, *Handbook of Conveying and Handling of Particulate Solids*, pages 39–44, Amsterdam, The Netherlands. Elsevier.

Luding, S., Nicolas, M., and Pouliquen, O. (2000). A minimal model for slow dynamics: Compaction of granular media under vibration or shear. In Kolymbas, D. and Fellin, W., editors, *Compaction of Soils, Granulates and Powders*, pages 241–249, Rotterdam. A. A. Balkema.

Luding, S., Tykhoniuk, R., and Tomas, J. (2003). Anisotropic material behavior in dense, cohesive powders. *Chem. Eng. Technol.*, 26(12):1229–1232.

Manetsberger, K., Shen, J., and Muellers, J. (2001). Compensation of nonlinear shrinkage of polymer materials in selective laser sintering. In *Solid Freeform Fabrication Symposium*, pages 221–232.

Olevsky, E. A. (1998). Theory of sintering: from discrete to continuum. *Materials Science and Engineering*, R23:41–100.

Redanz, P. and Fleck, N. A. (2001). The compaction of a random distribution of metal cylinders by the discrete element method. *Acta Materialia*, 49:4325–4335.

Riedel, H. and Blug, B. (2001). A comprehensive model for solid state sintering and its application to silicon carbide. In Chuang, T.-J. and Rudnicki, J. W., editors, *Multiscale deformation and fracture in materials and structures, the James R. Rice 60th anniversary volume, Solid mechanics and its application - Vol. 84*, pages 49–70, Dordrecht. Kluwer Academic Publishers.

Riedel, H., Zipse, H., and Svoboda, J. (1994). Equilibrium pore surfaces, sintering stresses and constitutive equations for the intermediate and late stages of sintering - II. diffusional densification and creep. *Acta Metall. Mater.*, 42:445–452.

Sadd, M. H., Tai, Q. M., and Shukla, A. (1993). Contact law effects on wave propagation in particulate materials using distinct element modeling. *Int. J. Non-Linear Mechanics*, 28(2):251.

Schwedes, J. (1968). *Fließverhalten von Schüttgütern in Bunkern.* Verlag Chemie, Weinheim.

Svoboda, J., Riedel, H., and Zipse, H. (1994). Equilibrium pore surfaces, sintering stresses and constitutive equations for the intermediate and late stages of sintering - I. computation of equilibrium surfaces. *Acta Metall. Mater.*, 42:435–443.

Thornton, C. (2000). Numerical simulations of deviatoric shear deformation of granular media. *Géotechnique*, 50(1):43–53.

Thornton, C. and Antony, S. J. (2000). Quasi-static deformation of a soft

particle system. *Powder Technology*, 109(1-3):179–191.

Tomas, J. (2000). Particle adhesion fundamentals and bulk powder consolidation. *KONA*, 18:157–169.

van Baars, S. (1996). *Discrete Element Analysis of Granular Materials*. PhD thesis, Technische Universiteit Delft, Delft, Nederlands.

Vermeer, P. A., Diebels, S., Ehlers, W., Herrmann, H. J., Luding, S., and Ramm, E., editors (2001). *Continuous and Discontinuous Modelling of Cohesive Frictional Materials*, Berlin. Springer. Lecture Notes in Physics 568.

Walton, O. R. and Braun, R. L. (1986). Viscosity, granular-temperature, and stress calculations for shearing assemblies of inelastic, frictional disks. *Journal of Rheology*, 30(5):949–980.

Zachariah, M. R. and Carrier, M. J. (1999). Molecular dynamics computation of gas-phase nanoparticle sintering: A comparison with phenomenological models. *J. Aerosol Science*, 30(9):1139–1151.

Zhu, C. Y., Shukla, A., and Sadd, M. H. (1991). Prediction of dynamic contact loads in granular assemblies. *J. of Applied Mechanics*, 58:341.